NASA Contractor Report 189224

Numerical Simulation of Geometric Scale Effects in Cylindrical Self-Field MPD Thrusters

M. LaPointe
Sverdrup Technology, Inc.
Lewis Research Center Group
Brook Park, Ohio

Prepared for the
28th Joint Propulsion Conference and Exhibit
cosponsored by the AIAA, SAE, ASME, and ASEE
Nashville, Tennessee, July 6–8, 1992

Numerical Simulation of Geometric Scale Effects in Cylindrical Self-Field MPD Thrusters

Michael R. LaPointe[1]
Sverdrup Technology, Inc., Brook Park, Ohio 44142

Abstract

A two-dimensional, two-temperature, single fluid magnetohydrodynamics code which incorporates classical plasma transport coefficients and Hall effects has been developed to predict steady-state, self-field MPD thruster performance. The governing equations and numerical methods of solution are outlined and discussed. Experimental comparisons are used to validate model predictions. The model accurately predicts thrust and reproduces trends in the discharge voltage for discharge currents below experimentally measured onset values. However, because the model does not include electrode effects the calculated voltage drops are significantly lower than experimentally measured values. Predictions of thrust and flow efficiency are made for a matrix of fifteen cylindrical thruster geometries assuming a fully ionized argon propellant. A maximum predicted specific impulse of 1680 s is obtained for a thruster with an anode radius of 2.5 cm, a cathode radius of 0.5 cm, and equal electrode lengths of 2.5 cm. A scaling relation is developed to predict, within limits, the onset of cylindrical, self-field thruster instability as a function of geometry and operating condition.

Nomenclature

A	plasma ionization function	$v_{0,(exit)}$	inlet (exit) velocity, m/s
A_e	thruster exit area, m^2	V	discharge voltage, V
$\vec{B}$	magnetic field, T	V_{out}	external volume, m^3
e	electric charge, C	V_{tot}	total volume, m^3
$\vec{E}$	electric field, V/m	α_n	finite difference coeffs.
F	thrust, N	γ_n	differential equation coeffs.
g	gravitational acceleration, 9.8 m/s^2	Γ_m^n	differential equation coeffs.
I_{sp}	specific impulse, s	ϵ_0	permittivity of free space, 8.854×10^{-12} $C^2/N\text{-}m^2$
$\vec{j}$	current density, A/m^2	η	viscosity, kg/m-s
J	discharge current, A	η_f	plasma flow efficiency
$l_{a,c}$	length (anode,cathode), m	$\kappa_{i(e)}$	ion (electron) thermal conductivity, Watt/m-K
k_B	Boltzmann const., J/K	λ	second coeff. of viscosity, kg/m-s
m, M	electron, ion mass, kg	$\ln \Lambda_{i(e)}$	ion (electron) Coulomb logarithm
$\dot{m}$	mass flow rate, kg/s	μ_0	permeability of free space
n	number density, m^{-3}	ν_{ei}	electron-ion collision frequency, s^{-1}
$p_{(i,e)}$	pressure (ion, electron), Pa	ξ	density function
p_{exit}	exit plane pressure, Pa	ρ	mass density, kg/m^3
p_{tank}	background gas pressure, Pa	σ	electrical conductivity, mho/m
P	power, W	τ_e	electron collision time, s
ΔQ_{ei}	energy exchange term, J/s	ϕ	electric potential, V
$r_{(a,c)}$	radius (anode, cathode), m	Φ_V	viscous dissipation function
R	gas constant, J/K-mol	ψ	magnetic field streamline
S	general source term	$\vec{\Psi}$	viscous force vector
S_{tc}	thrust chamber inner surface, m^2	ω	convergence factor
$T_{i(e)}$	ion (electron) temperature, K	ω_{ce}	electron cyclotron frequency, s^{-1}
$\vec{v}$	velocity, m/s	Ω	electron Hall parameter

Subscripts:

i, e	ion, electron
r, θ, z	radial coordinates

[1]Senior Propulsion Engineer, Member, AIAA

I. Introduction

The magnetoplasmadynamic (MPD) thruster has been advocated for a variety of propulsion applications, from near-Earth orbit raising maneuvers[1] to the long duration interplanetary missions envisioned by the National Space Exploration Initiative.[2] In its basic form, the MPD thruster consists of a cylindrical cathode surrounded by a concentric anode (Figure 1). An arc struck between the electrodes ionizes a gaseous propellant, and the interaction of the current with the self-induced magnetic field accelerates the plasma to produce thrust. Steady-state MPD thrusters have been operated at power levels approaching 600 kW, while pulsed, quasi-steady devices have operated in the megawatt power range.[3] The engine is robust and designed to provide low, continuous thrust at specific impulse values between 1,000 and 10,000 s.

MPD thruster performance is currently limited by low thrust efficiency in the operating regimes of interest,[3,4,5] with significant fractions of the applied power deposited into the anode. For low power steady-state thrusters, the anode power fraction may reach 80%, leaving only 20% for plasma ionization and acceleration.[3] Experimentally, the use of applied magnetic fields[3,4] and flared electrode geometries[6] have been shown to increase the specific impulse and improve thruster efficiency, although for reasons poorly understood at present. The specific impulse for a self-field MPD thruster is related to $J^2/\dot{m}$, a parameter which is often used to characterize MPD thruster performance.[3] High values of $J^2/\dot{m}$ correspond to predominantly electromagnetic acceleration, and provide higher values of specific impulse; low values of $J^2/\dot{m}$ correspond to predominantly electrothermal acceleration, and lower values of specific impulse. MPD thruster efficiency typically increases with increasing $J^2/\dot{m}$, but is limited by the occurrence of discharge voltage oscillations which result in severe electrode erosion. Several mechanisms have been proposed to explain the onset of these instabilities, including anode mass starvation,[7] flow choking due to enhanced back-EMF,[8,9] and the triggering of electrothermal and gradient-driven instabilities as the plasma approaches full ionization.[10,11,12] It appears that different operating conditions may trigger one or a combination of the proposed mechanisms, with a concomitant reduction in thruster performance and lifetime.

MPD thrusters have undergone extensive experimental development since the 1960's,[3-5] but a comprehensive theoretical analysis has been hampered by the complex nature of the coupled electromagnetic and gasdynamic acceleration processes. Analytic and numerical simulations using 1D and quasi-1D approximations of the magnetohydrodynamic fluid equations have provided valuable insights into both self-field and applied-field MPD thruster operation, but they are by definition constrained in their ability to predict detailed thruster performance. The removal of such limitations via 2D and quasi-2D modeling has become practical with the emergence of high-speed computational facilities, allowing model validation and refinement using the existing experimental data base, while in return establishing a theoretical basis to guide further experimentation. A review of MPD thruster technology and a survey of recent MPD thruster models is provided by Myers *et al.*.[3]

Self-Field MPD Thruster Scaling Studies.

Steady improvements in MPD thruster performance have occurred primarily via the relatively expensive method of device fabrication and testing, with the more robust designs surviving this evolutionary process to undergo further testing and refinement. However, with the variety of thruster geometries currently under development, progress toward understanding the impact of geometric scaling on performance has been delayed by an incomplete empirical data base and by the replication of experimental effort. The limited research efforts which address performance variations due to geometric changes in the electrode shapes are reviewed below.

One of the first comprehensive attempts to verify the effects of geometric variation on MPD thruster performance was reported by King,[13] who combined an experimental approach with a simplified 1D gasdynamic

model to evaluate anode modifications in the Princeton benchmark thruster. King found that increased electrode lengths and decreased anode radii allow an increase in the discharge current before the onset of thruster instability, with the decreased anode orifice contributing most strongly to the increased stability. The results led to the design of a modified flared anode thruster, which consisted of two straight anode channels connected by a flared anode region. The design proved to have equivalent voltage-current characteristics and a slightly higher thrust efficiency compared to a straight cylindrical MPD thruster of similar dimensions.

In a detailed experimental study, Gilland[14] compared the performance of the Princeton standard benchmark thruster and the modified flared anode thruster with their geometric half-scale counterparts. In each case, thruster performance was determined to be primarily a function of propellant mass flow rate and the ratio of the electrode radii, but was generally independent of the geometric scale of the thruster. The scaled thruster performance was similar for similar mass flow rates, although the half scale thrusters were less efficient at equal power levels and exhaust velocities.

Schmidt[15] combined an empirical approach with a simple theoretical model to analyze the full scale and half scale Princeton benchmark and flared anode thrusters. Empirical data were employed to generate an analytic expression for voltage scaling in the devices. An expression was assumed for the current density distribution and used to evaluate thruster force components. An analytic expression was used to estimate the contributions by electrothermal forces, and the model was employed to analyze the performance of the full scale and half scale thrusters. The half scale thrusters, operated at half the power levels of the full scale versions, were found to have similar efficiencies and increased specific impulse, in general agreement with the experimental findings of Gilland. The model was to be used in conjunction with an Air Force Rocket Propulsion Laboratory (now Air Force Phillips Laboratory) experimental program to develop a variable geometry MPD thruster, designed specifically to address geometric scaling issues. Cassady *et al.*[16] provide a brief description of the program, but little information has been published in the intervening years.

Heimerdinger[17] performed an experimental evaluation of two thruster geometries, one a straight cylindrical channel and the second a straight cylindrical channel with diverging area near the exit plane. The constant area channel suffered from strong current concentrations near the inlet and exit regions, resulting in enhanced electrode erosion. The diverging electrode geometry diminished the discharge current densities and reduced the electrode erosion, and demonstrated that electrode geometries could be tailored to minimize ohmic heating and associated electrode erosion.

Martinez-Sanchez[18] developed an analytic model using steady-state, quasi-1D MHD flow equations, and evaluated a variety of electrode geometries. Optimum performance was obtained with a converging-diverging anode, which allowed more uniform current concentration along the electrodes. In descending order of performance were geometries which employed a diverging anode, a converging anode, and a straight cylindrical anode. The poor performance of the cylindrical electrode geometry was due to thermal pressure effects retarding the flow near the exit plane of the thruster. The results confirmed that electrode contouring can be effective in controlling the current distribution and associated energy dissipation effects.

The experimental results of Kunii *et al.*[19] confirmed that straight cylindrical thruster geometries did indeed suffer from current concentrations near the base and tip of the cathode, with subsequent severe cathode erosion. A diverging anode was found to produce the most uniform current distribution; however, a converging-diverging anode showed severe current concentrations and electrode erosion, in contrast to the analytic models discussed above. In a comparison of cylindrical and flared thruster geometries, Uematsu *et al.*[20] demonstrated that the performance of a straight cylindrical thruster was improved by recessing the cathode, at the expense of increasing the cathode erosion rate. The flared anode thrusters were again shown to provide better performance, with better stability and less erosion, than cylindrical electrode geometries. In a recent modeling effort, Lefever-Button and Subramaniam[21] employed a quasi-1d model with finite rate kinetics to compare cylindrical and flared thruster geometries. For fixed operating conditions, the flared ge-

ometries produced higher exhaust velocities, reduced the current density concentrations near the exit plane, and increased the propellant ionization fraction compared to straight cylindrical thruster geometries.

Preble[10] compiled a comprehensive data base of experimentally determined onset values for self-field, cylindrical MPD thrusters operated with argon propellants. A stability model, developed to simulate the onset of electrothermal instabilities, was combined with a one-dimensional MHD code and used to evaluate onset conditions for a variety of thruster scale lengths. Through an extensive literature search, Preble catalogued several mechanisms which could lead to improved thruster performance. Longer electrode lengths, smaller interelectrode spacing, and propellant injection near the anode were found to significantly increase the value of $J^2/\dot{m}$ before the onset of thruster instability, allowing thrusters to operate more efficiently with higher specific impulse. The trends predicted by the model correlated very well with experimentally determined onset conditions, and demonstrated that an electrothermal instability could precipitate global thruster instability over the range of geometric scales considered in the study.

In addition to the onset of global thruster instability, plasma microinstabilities may arise which lead to an increase in the plasma resistivity, raising the voltage drop across the plasma and lowering thruster efficiency. Niewood *et al.*[11] combined a quasi-1D flow model with nonlinear dispersion relations to show that modified two-stream and electrothermal instabilities may arise in MPD thruster plasmas, with the onset of operational instability closely coupled to the occurrence of the electrothermal instability. Choueiri[22] and Choueiri *et al.*[23] derived general nonlinear dispersion relations for current-driven plasma instabilities, and determined that lower-hybrid waves are the dominant microinstability for most MPD thruster operating regimes. The existence of lower-hybrid waves has been experimentally verified in both low power and high power MPD thrusters.[22,24]

Although limited in extent, significant information has been obtained from the experimental and numerical scaling studies outlined above. In general, flared electrode geometries provide more uniform current distributions, reduce electrode erosion, and enhance thruster stability. Straight cylindrical thrusters appear to operate more stably with longer electrodes, smaller interelectrode separations, and propellant injection near the anode. Half-scale reductions in thruster size might not significantly alter thruster performance for equal mass flow rates, although half-scale geometries are less efficient at equal power levels and exhaust velocities. Unfortunately, this impressive list of maxims is not yet sufficient to guide thruster designs toward an optimal configuration. Several uncertainties remain, such as the optimum scaling of electrode length versus thruster diameter, the impact of electrode length on thruster performance and efficiency, and the combined effect of geometric scale and operating condition on MPD thruster stability. The two-temperature MPD thruster model described below has been employed in an effort to address some of these lingering issues for cylindrical, self-field MPD thrusters.

II. Two-Temperature MPD Thruster Model

The two-temperature MPD thruster model is an extension of the single fluid, single temperature MPD code discussed in Reference [25]. Separate electron and ion energy equations have been incorporated into the steady-state, viscous, compressible, single fluid magnetohydrodynamic equations, which are written in cylindrical coordinates with assumed symmetry about the centerline. The plasma is assumed to be fully, singly ionized, and is described by a perfect gas equation of state. The inclusion of separate electron and ion temperatures permits refined calculations of the classical plasma transport coefficients, which provide more accurate estimates of the plasma voltage drop, viscous flow losses, and thruster efficiency.

IIa. Electromagnetic Field Equations.

The basic set of electromagnetic equations includes the full complement of Maxwell's equations:

$$(a)\ \nabla \cdot \vec{B} = 0 \qquad (b)\ \nabla \times \vec{B} = \mu_0 \vec{j} \tag{1}$$

$$(c)\ \nabla \cdot \vec{E} = \rho_e/\epsilon_0 \approx 0 \qquad (d)\ \nabla \times \vec{E} = -\frac{\partial \vec{B}}{\partial t} = 0$$

which incorporate the steady-state, single fluid plasma approximations. A general Ohm's law of the form:

$$\vec{j} = \sigma\left[\vec{E} + \left(\vec{v} \times \vec{B}\right)\right] - \frac{\Omega}{B}\left(\vec{j} \times \vec{B}\right) \tag{2}$$

is used to relate the current density $\vec{j}$ to the plasma velocity $\vec{v}$ and the electric ($\vec{E}$) and magnetic ($\vec{B}$) fields. Ion slip terms are neglected due to the assumption of full ionization. The electrical conductivity σ is given by the classical Spitzer-Harm conductivity for a fully ionized plasma:[26]

$$\sigma = 1.53 \times 10^{-2}\frac{T^{3/2}}{\ln \Lambda_e} \tag{3}$$

where T_e is the electron temperature in degrees-Kelvin, $\ln\Lambda_e$ is the electron Coulomb logarithm:

$$\ln \Lambda_e \approx 23 - ln\left[\frac{1.22 \times 10^3 n^{1/2}}{T_e^{3/2}}\right] \tag{4}$$

and n is the (single fluid) plasma number density expressed in particles per cubic meter. The electron Hall parameter Ω is the product of the electron cyclotron frequency (ω_{ce}) and the electron collision time (τ_e):

$$\begin{aligned} \Omega = \omega_{ce}\tau_e &= \left(\frac{eB}{m}\right)\cdot\left(\frac{m\sigma}{ne^2}\right) \\ &= 9.6 \times 10^{16}\left(\frac{T_e^{3/2}B}{Zn\ln\Lambda}\right) \end{aligned} \tag{5}$$

where m is the electron mass, e is the electron charge, and B is the magnitude of the local magnetic field.

Equation 2 may be rearranged to solve for the electric field distribution:

$$\vec{E} = -\nabla\phi = \frac{1}{\sigma}\left[\vec{j} + \frac{\Omega}{B}\left(\vec{j} \times \vec{B}\right)\right] - \left(\vec{v} \times \vec{B}\right) \tag{6}$$

whose components are given by:

$$\begin{aligned} E_r &= -\frac{\partial\phi}{\partial r} = \frac{1}{\sigma}\left[j_r + \frac{\Omega}{B}\left(j_\theta B_z - j_z B_\theta\right)\right] - \left(v_\theta B_z - v_z B_\theta\right) \\ E_\theta &= -\frac{\partial\phi}{\partial\theta} \equiv 0 \\ E_z &= -\frac{\partial\phi}{\partial z} = \frac{1}{\sigma}\left[j_z + \frac{\Omega}{B}\left(j_r B_\theta - j_\theta B_r\right)\right] - \left(v_r B_\theta - v_\theta B_r\right) \end{aligned} \tag{7}$$

The radial electric field is integrated from cathode to anode to find the potential drop ϕ across the plasma. The divergence of Eq. 6 may be used to generate a Poisson equation for the potential, or assuming quasineutrality a simple Laplace equation may be solved to give the potential distribution, with the calculated plasma fall providing the necessary boundary conditions. The first method is rigorously correct, while the second method is computationally faster; both have been tested, and yield essentially identical results for the plasma potential distribution.

A magnetic transport equation may be derived by combining Maxwell's equations with the generalized Ohm's law:

$$\begin{aligned} \nabla \times \vec{E} &= -\frac{\partial \vec{B}}{\partial t} \\ &= \nabla \times \left(\frac{\nabla \times \vec{B}}{\mu_0\sigma}\right) + \nabla \times \left[\frac{\Omega}{\mu_0\sigma B}\left((\nabla \times \vec{B}) \times \vec{B}\right)\right] - \nabla \times \left(\vec{v} \times \vec{B}\right) = 0 \end{aligned} \tag{8}$$

Defining $\beta = \Omega/(\sigma B)$ and $\psi = rB_\theta$, the azimuthal component of the above equation can be written:

$$\frac{\partial^2\psi}{\partial r^2} + \gamma_1\frac{\partial\psi}{\partial r} + \gamma_2\frac{\partial\psi}{\partial z} + \gamma_3\psi + \frac{\partial^2\psi}{\partial z^2} = S \tag{9}$$

where

$$\begin{aligned}
\gamma_1 &= -\left(\frac{1}{r} + \frac{1}{\sigma}\frac{\partial\sigma}{\partial r} - \psi\frac{\sigma}{r}\frac{\partial\beta}{\partial z} + \mu_0\sigma v_r\right) \\
\gamma_2 &= \left(-\frac{1}{\sigma}\frac{\partial\sigma}{\partial z} - \psi\frac{2\beta\sigma}{r^2} + \psi\frac{\sigma}{r}\frac{\partial\beta}{\partial r} + \mu_0\sigma v_z\right) \\
\gamma_3 &= -\left(\mu_0\sigma\left[\frac{\partial v_r}{\partial r} - \frac{v_r}{r} + \frac{\partial v_z}{\partial z}\right]\right)
\end{aligned} \tag{10}$$

where the source term S incorporates effects of an applied magnetic field, and is equal to zero for the self-field thruster under consideration. Once the magnetic transport equation is solved for ψ, the value of B_θ is readily obtained. The azimuthal magnetic field is a function of the total discharge current J, and through the relation $\psi = rB_\theta \sim r(J/r) \sim J$, the function $\psi(r,z) = constant$ may be used to represent lines of total enclosed current.

Returning to the Maxwell equations, the radial and axial current densities are obtained from the calculated magnetic field distributions:

$$\begin{aligned}
j_r &= -\frac{1}{\mu_0}\frac{\partial B_\theta}{\partial z} \\
j_z &= \frac{1}{\mu_0}\left(\frac{1}{r}\frac{\partial}{\partial r}\left(rB_\theta\right)\right)
\end{aligned} \tag{11}$$

The azimuthal current density j_θ vanishes due to the absence of applied radial or axial magnetic fields in the self-field MPD thruster.

IIb. Fluid Equations.

The fluid equations are based on the conservation equations of mass, momentum, and energy. Conservation of mass for a compressible fluid is given by:

$$\nabla\cdot(\rho\vec{v}) = 0 \tag{12}$$

which can be written:

$$\frac{\partial\left(r\rho v_r\right)}{\partial r} + \frac{\partial\left(r\rho v_z\right)}{\partial z} = 0 \tag{13}$$

where ρ is the plasma mass density. Defining $\xi = r\rho$, the mass conservation equation takes the simplified form:

$$\frac{\partial\xi v_r}{\partial r} + \frac{\partial\xi v_z}{\partial z} = 0 \tag{14}$$

which is solved for ξ, from which the value of ρ is determined.

Momentum. The conservation of momentum, including viscosity, is expressed in vector form as:

$$\rho\left(\vec{v}\cdot\nabla\right)\vec{v} = -\nabla p + \left(\vec{j}\times\vec{B}\right) + \vec{\Psi} \tag{15}$$

where p is the plasma pressure and $\vec{\Psi}$ is the viscous force vector:

$$\vec{\Psi} = -\frac{2}{3}\nabla\left[\eta\left(\nabla\cdot\vec{v}\right)\right] + \eta\left[\nabla^2\vec{v} + \nabla\left(\nabla\cdot\vec{v}\right)\right] + 2\left(\nabla\eta\cdot\nabla\right)\vec{v} + \nabla\eta\times\left(\nabla\times\vec{v}\right) \tag{16}$$

The viscosity η for a fully ionized plasma is given by:[27]

$$\eta = 1.25\times10^{-19}\frac{5}{8n^{i}A}\left(\frac{Mmk_BT_i}{\pi}\right)^{1/2}\left(\frac{2k_BT_i}{e^2}\right)^2 \tag{17}$$

where T_i is the ion temperature, M is the ion mass, m is the electron mass, e is the electron charge, k_B is Boltzmann's constant, n^i=1 for a singly ionized plasma, and, for a fully ionized gas ($\alpha = 1$),

$$A = 2\left[\ln\left(1+\alpha^2\right) - \frac{\alpha^2}{1+\alpha^2}\right] = 0.386$$

The radial component of the momentum equation is used to solve for the radial velocity v_r:

$$\begin{aligned}\rho\left(v_r\frac{\partial v_r}{\partial r} + v_z\frac{\partial v_r}{\partial z} - \frac{v_\theta^2}{r}\right) &= -\frac{\partial p}{\partial r} + -j_zB_\theta - v_r\left(\frac{4}{3}\frac{\eta}{r^2} + \frac{2}{3r}\frac{\partial\eta}{\partial r}\right) + \frac{4}{3}\frac{\partial v_r}{\partial r}\left(\frac{\eta}{r} + \frac{\partial\eta}{\partial r}\right)\\ &+ \frac{\partial v_r}{\partial z}\frac{\partial\eta}{\partial z} + \frac{4\eta}{3}\frac{\partial^2 v_r}{\partial r^2} + \eta\frac{\partial^2 v_r}{\partial z^2} + \frac{\eta}{3}\frac{\partial^2 v_z}{\partial r\partial z} + \frac{\partial\eta}{\partial z}\frac{\partial v_z}{\partial r} - \frac{2}{3}\frac{\partial\eta}{\partial r}\frac{\partial v_z}{\partial z}\end{aligned} \tag{18}$$

and may be recast in the form:

$$\eta\frac{\partial^2 v_r}{\partial r^2} + \Gamma_r^1\frac{\partial v_r}{\partial r} + \Gamma_r^2\frac{\partial v_r}{\partial z} - \Gamma_r^3 v_r + \frac{3\eta}{4}\frac{\partial^2 v_r}{\partial z^2} = -S_r \tag{19}$$

where

$$\begin{aligned}\Gamma_r^1 &= \left(\frac{\eta}{r} + \frac{\partial\eta}{\partial r} - \frac{3\rho v_r}{4}\right)\\ \Gamma_r^2 &= \frac{3}{4}\left(\frac{\partial\eta}{\partial z} - \rho v_z\right)\\ \Gamma_r^3 &= \left(\frac{\eta}{r^2} + \frac{1}{2r}\frac{\partial\eta}{\partial r}\right)\end{aligned} \tag{20}$$

and

$$S_r = \frac{3}{4}\left(-\frac{\partial p}{\partial r} - j_zB_\theta + \frac{\eta}{3}\frac{\partial^2 v_z}{\partial r\partial z} + \frac{\partial\eta}{\partial z}\frac{\partial v_z}{\partial r} - \frac{2}{3}\frac{\partial\eta}{\partial r}\frac{\partial v_z}{\partial z} + \frac{\rho v_\theta^2}{r}\right) \tag{21}$$

There are no radial or axial magnetic fields in the self-field MPD thruster, hence no azimuthal momentum is generated. The axial momentum component is given by:

$$\begin{aligned}\rho\left(v_r\frac{\partial v_z}{\partial r} + v_z\frac{\partial v_z}{\partial z}\right) &= -\frac{\partial p}{\partial z} + j_rB_\theta + \eta\frac{\partial^2 v_z}{\partial r^2} + \left(\frac{\eta}{r} + \frac{\partial\eta}{\partial r}\right)\frac{\partial v_z}{\partial r} + \frac{4}{3}\frac{\partial\eta}{\partial z}\frac{\partial v_z}{\partial z}\\ &+ \frac{4\eta}{3}\frac{\partial^2 v_z}{\partial z^2} + \frac{\partial v_r}{\partial z}\left(\frac{\eta}{3r} + \frac{\partial\eta}{\partial r}\right) - \frac{2}{3}\frac{\partial\eta}{\partial z}\left(\frac{v_r}{r} + \frac{\partial v_r}{\partial r}\right) + \frac{\eta}{3}\frac{\partial^2 v_r}{\partial r\partial z}\end{aligned} \tag{22}$$

which yields an equation for the axial velocity v_z:

$$\eta\frac{\partial^2 v_z}{\partial r^2} + \Gamma_z^1\frac{\partial v_z}{\partial r} + \Gamma_z^2\frac{\partial v_z}{\partial z} + \frac{4\eta}{3}\frac{\partial^2 v_z}{\partial z^2} = -S_z \tag{23}$$

where

$$\begin{aligned} \Gamma_z^1 &= \left(\frac{\eta}{r} + \frac{\partial \eta}{\partial r} - \rho v_r\right) \\ \Gamma_z^2 &= \left(\frac{4}{3}\frac{\partial \eta}{\partial z} - \rho v_z\right) \end{aligned} \tag{24}$$

and

$$S_z = -\frac{\partial p}{\partial z} + j_r B_\theta + \frac{\partial v_r}{\partial z}\left(\frac{\eta}{3r} + \frac{\partial \eta}{\partial r}\right) - \frac{2}{3}\frac{\partial \eta}{\partial z}\left(\frac{v_r}{r} + \frac{\partial v_r}{\partial r}\right) + \frac{\eta}{3}\frac{\partial^2 v_r}{\partial r \partial z} \tag{25}$$

Energy. The electron and ion energy equations are adapted from Mitchner and Kruger,[27] converted to steady-state form, and rewritten in terms of the plasma mass density. Grouping terms by order, the electron energy equation may be written:

$$\kappa_e \frac{\partial^2 T_e}{\partial r^2} + \Gamma_e^1 \frac{\partial T_e}{\partial r} + \Gamma_e^2 \frac{\partial T_e}{\partial z} - \Gamma_e^3 T_e + \kappa_e \frac{\partial^2 T_e}{\partial z^2} = -S_e \tag{26}$$

where T_e is the electron temperature, κ_e is the Spitzer-Harm electron thermal conductivity:[26]

$$\kappa_e = \frac{75(4\pi\varepsilon_0)^2 k_B (k_B T_e)^{5/2}}{32\pi^{1/2} m^{1/2} e^4 \ln \Lambda_e} \approx 2.55 \times 10^{-10} \frac{T_e^{5/2}}{\ln \Lambda_e} \tag{27}$$

and the equation coefficients are:

$$\begin{aligned} \Gamma_e^1 &= \frac{\kappa_e}{r} + \frac{\partial \kappa_e}{\partial r} - \frac{3}{2}\rho R v_r \\ \Gamma_e^2 &= \frac{\partial \kappa_e}{\partial z} - \frac{3}{2}\rho R v_z \\ \Gamma_e^3 &= \rho R\left(\frac{v_r}{r} + \frac{\partial v_r}{\partial r} + \frac{\partial v_z}{\partial z}\right) \end{aligned} \tag{28}$$

The electron energy source term S_e is given by:

$$S_e = \vec{j} \cdot (\vec{E} + \vec{v} \times \vec{B}) - \Delta Q_{ei} \tag{29}$$

where the first term on the right represents joule heating of the plasma electrons, and the second term represents an energy exchange between the electrons and plasma ions:

$$\Delta Q_{ei} = 3\frac{m}{M}\rho R(T_e - T_i)\nu_{ei} \tag{30}$$

with the electron-ion collision frequency given by:

$$\nu_{ei} = 1.836 \times 10^{-6} \frac{\rho \ln \Lambda_e}{M T_e^{3/2}}$$

The steady-state ion energy equation takes the form:

$$\kappa_i \frac{\partial^2 T_i}{\partial r^2} + \Gamma_i^1 \frac{\partial T_i}{\partial r} + \Gamma_i^2 \frac{\partial T_i}{\partial z} - \Gamma_i^3 T_i + \kappa_i \frac{\partial^2 T_i}{\partial z^2} = -S_i \tag{31}$$

where T_i is the ion temperature, κ_i is the Spitzer-Harm ion thermal conductivity:

$$\kappa_i = 1.35 \times 10^{-12} \frac{T_i^{5/2}}{\ln \Lambda_i} \tag{32}$$

and the equation coefficients are:

$$\begin{aligned} \Gamma_i^1 &= \frac{\kappa_i}{r} + \frac{\partial \kappa_i}{\partial r} - \frac{3}{2}\rho R v_r \\ \Gamma_i^2 &= \frac{\partial \kappa_i}{\partial z} - \frac{3}{2}\rho R v_z \\ \Gamma_i^3 &= \rho R \left(\frac{v_r}{r} + \frac{\partial v_r}{\partial r} + \frac{\partial v_z}{\partial z} \right) \end{aligned} \tag{33}$$

The ion energy source term S_i is given by:

$$S_i = \Phi_V + \Delta Q_{ei} \tag{34}$$

where the first term on the right represents ion heating by viscous dissipation, and the second term again represents the energy exchange between the electrons and ions. Joule heating of the ions is neglected in the ion source term, as it is assumed the ion current density is substantially smaller than the electron current density.

The viscous dissipation Φ_V is:[26]

$$\Phi_V = \eta \left(2 \left[\left(\frac{\partial v_r}{\partial r} \right)^2 + \left(\frac{v_r}{r} \right)^2 + \left(\frac{\partial v_z}{\partial z} \right)^2 \right] + \left(\frac{\partial v_\theta}{\partial z} \right)^2 + \left(\frac{\partial v_r}{\partial z} + \frac{\partial v_z}{\partial r} \right)^2 + \left(\frac{\partial v_\theta}{\partial r} - \frac{v_\theta}{r} \right)^2 \right) + \lambda \left(\frac{\partial v_r}{\partial r} + \frac{v_r}{r} + \frac{\partial v_z}{\partial z} \right)^2 \tag{35}$$

where λ represents the second coefficient of viscosity for a monatomic gas:

$$\lambda + \frac{2}{3}\eta = 0 \tag{36}$$

The set of fluid equations are closed with an ideal gas equation of state relating the plasma pressure, density, and temperature:

$$p = (p_i + p_e) = \rho R (T_i + T_e) \tag{37}$$

IIc. Finite Difference Formulation

The governing equations have the general form:

$$f = \alpha_1 \frac{\partial^2 Y}{\partial r^2} + \alpha_2 \frac{\partial Y}{\partial r} + \alpha_3 \frac{\partial Y}{\partial z} + \alpha_4 \frac{\partial^2 Y}{\partial z^2} + \alpha_0 Y + S \tag{38}$$

where the α_n denote nonconstant coefficients and S represents a possible source term. The coupled form of the equations hinders an analytic solution, and suggests the use of an iterative numerical approach. The equations are written in finite difference form, and solved on a uniform rectangular grid using a generalized Newton-Raphson iteration method.[28] Second derivatives are represented by a second-order central difference formulation:

$$\begin{aligned} \frac{\partial^2 Y}{\partial r^2} &= \frac{Y(j,i+1) - 2Y(j,i) + Y(j,i-1)}{(\Delta r)^2} \\ \frac{\partial^2 Y}{\partial z^2} &= \frac{Y(j+1,i) - 2Y(j,i) + Y(j-1,i)}{(\Delta z)^2} \end{aligned} \tag{39}$$

where the index j represents nodal points along the axial grid direction, i represents nodal points along the radial grid direction, and Δr and Δz are the radial and axial grid spacings, respectively. First derivatives are written using a first-order switching scheme, which is based upon the sign of the coefficients multiplying the derivatives:[28]

$$\frac{\partial Y}{\partial r} = \begin{cases} \frac{Y(j,i+1)-Y(j,i)}{\Delta r} & \alpha_2 \geq 0 \\ \frac{Y(j,i)-Y(j,i-1)}{\Delta r} & \alpha_2 < 0 \end{cases}$$

$$\frac{\partial Y}{\partial z} = \begin{cases} \frac{Y(j+1,i)-Y(j,i)}{\Delta z} & \alpha_3 \geq 0 \\ \frac{Y(j,i)-Y(j-1,i)}{\Delta z} & \alpha_3 < 0 \end{cases} \tag{40}$$

This scheme preserves the dominance of the $Y(j,i)$ term and assures stability of the numerical solution.

Once written in their finite difference analogs, each equation is regrouped into the general form:

$$X = a_0 Y(j,i) + a_1 Y(j,i+1) + a_2 Y(j,i-1) + a_3 Y(j+1,i) + a_4 Y(j-1,i) + S(j,i) \tag{41}$$

where the a_n are nonconstant coefficients, which must be evaluated at each grid location. The generalized Newton-Raphson iteration method

$$Y(j,i) = Y(j,i) - \omega \frac{F}{[\partial F / \partial Y(j,i)]} \tag{42}$$

is then used to iteratively solve each finite difference equation. An over-relaxation factor ω is used to speed convergence; its value lies between 1 and 2, and is determined through trial and error for each equation being solved.

Program execution is presented schematically in Figure 2. The fixed grid is divided into 50 radial by 100 axial nodes, and each equation is iterated first in the axial and then in the radial direction until a relative convergence criteria is satisfied (typically to within a tolerance of 10^{-4}). The process is repeated for each equation in turn, and the entire loop through the full set of equations is repeated until the exhaust velocity and plasma potential have each converged to within 1% of their previous loop values.

Thrust, Specific Impulse, and Flow Efficiency

Two complementary methods are used to calculate the total thrust, providing an independent check of the thrust value and allowing an estimate to be made of the various force components. The first method calculates the total electromagnetic thrust by numerically integrating the axial $\vec{j} \times \vec{B}$ body force over the total current carrying volume, including regions downstream of the thruster exit. Pressure forces generated within the thruster are numerically integrated over the inner surfaces of the thrust chamber, and combined with the electromagnetic thrust to estimate the total thrust:

$$F = \int_{V_{tot}} (\vec{j} \times \vec{B})_z dV_{tot} + \int_{S_{tc}} p dS_{tc} \tag{43}$$

where V_{tot} denotes the total current carrying volume and S_{tc} denotes surface regions within the thrust chamber.

A second thrust calculation is performed using:

$$F = \dot{m} v_{ex} + \int_{V_{out}} (\vec{j} \times \vec{B})_z dV_{out} + (p_{exit} - p_{tank}) A_e \tag{44}$$

The velocity at the exit plane of the thruster (v_{exit}) is given by:

$$v_{exit} = \frac{\sum_i \rho(ja,i) v_z^2(ja,i)}{\sum_i \rho(ja,i) v_z(ja,i)} \tag{45}$$

where the axial index ja denotes the anode exit plane and the radial integration extends from the thruster centerline to the inner anode radius. The integration of the electromagnetic body force is performed over the current carrying volume *external* to the thruster (V_{out}). The pressure force term corresponds to an imbalance between the pressure at the anode exit plane (p_{exit}) and the background gas pressure (p_{tank}), evaluated over the thruster exit area A_e. Note that the velocity at the thruster exit plane does not in general equal the MPD thruster exhaust velocity, due to the additional electromagnetic acceleration which may occur outside the thrust chamber and the imbalance of pressure forces at the exit plane.

Once the total thrust F is calculated, the specific impulse (I_{sp}) and plasma flow efficiency (η_f) are found via:

$$I_{sp} = \frac{F}{\dot{m}g} \qquad\qquad \eta_f = \frac{F^2}{(2\dot{m}P)} \tag{46}$$

where $\dot{m}$ is the propellant mass flow rate, g is the acceleration of gravity (9.8 m/s^2), and P is the power deposited in the plasma, equal to the plasma voltage multiplied by the discharge current. The model does not incorporate electrode effects, hence the total discharge voltage[†] necessary for a prediction of the total thruster efficiency cannot be calculated. Because electrode power losses may consume a significant portion of the total thruster power,[3] experimentally measured thruster efficiencies will generally be much lower than the calculated plasma flow efficiency η_f. Nevertheless, the flow efficiency provides a valuable benchmark against which various thruster geometries can be compared.

IId. Starting Values and Boundary Conditions

Code input consists of the thruster discharge current, propellant ion mass (amu), propellant mass flow rate, geometric boundary conditions, and a host of additional options such as maximum bulk electrode temperatures, background gas pressures (to model facility effects), and initial estimates for the plasma transport coefficients. Ion temperatures are typically set to 3000 K at electrode and insulator surfaces, and electron temperatures are assumed to be continuous into the surfaces ($\partial T_e/\partial n = 0$). Vacuum tank pressures are set between 1.3×10^{-2} and 1.3×10^{-4} Pa (10^{-4} and 10^{-6} torr, respectively). No appreciable difference is found in calculated thruster performance using either background pressure value. The inlet velocity v_0 is assumed to be sonic and uniform at the backplate. The inlet density ρ_0 is assumed to be uniform and is calculated from the 1-D continuity equation, $\dot{m} = \rho_0 v_0 A_0$, where A_0 is the exposed backplate surface area. Radial velocities are initially set to zero, and are defined by symmetry to remain zero along the centerline. Initial temperatures throughout the calculation region are set to the bulk electrode temperatures. Initial velocities and densities in the calculation region are set to their values at the backplate. A no-slip boundary condition on velocity is employed at all insulator and electrode surfaces.

The electrodes are modeled as equipotential surfaces. Electric fields which enter perpendicular to electrode surfaces satisfy the condition $\partial\vec{E}/\partial\hat{n}$=0, where $\hat{n}$ denotes a unit vector normal to the surface. Electric fields lying along electrode surfaces are set to zero, consistent with equipotential surface boundary conditions. Insulator surfaces support parallel electric fields, but zero current (due to an assumed infinite dielectric resistivity) and zero perpendicular electric fields (due to an assumed infinite relative dielectric permittivity). The magnetic stream line ψ is set equal to -$\mu_0 J/(2\pi)$ along the backplate, zero along the centerline, and is assumed to be continuous at both the outer radial grid boundary and and downstream axial grid boundary. Setting ψ=0 at the thruster exit plane would prevent the current from blowing out of the thruster, while setting ψ=0 at the downstream grid boundary might artificially compress the current blown downstream.

[†]The total discharge voltage is the sum of the plasma and electrode fall voltages.

To shorten loop convergence times, the temperature and velocity components are averaged with their previous loop values. This damps out minor fluctuations as a solution is approached, allowing more rapid loop convergence. Tests performed with and without smoothing yield essentially identical results. Model convergence with smoothing is typically obtained within 10-12 loops through the equations, requiring approximately 30 CPU minutes on a VAX-9000 computer. The code has not yet been optimized for a CRAY computing system.

III. Results and Discussion

Comparison with Experiment

The two-temperature self-field MPD thruster code was tested against the experimental performance of the Princeton University extended anode thruster.[29] The extended anode thruster, shown schematically in Figure 3, consists of a cylindrical 3.2 cm radius copper anode surrounding a 0.95 cm radius thoriated tungsten cathode. The anode and cathode lengths are 21.6 cm and 20 cm, respectively. Argon propellant is injected through an insulating boron nitride backplate, with either all of the propellant injected near the anode radius, or with half of the propellant injected through an annulus near the cathode base and half through a ring of 12 evenly spaced ports located 2 cm radially from the thruster centerline. For an argon mass flow rate of 6 g/s, the onset of thruster instability was observed to occur at a discharge current of approximately 21 kA for 50:50 propellant injection, and at approximately 41 kA for all-anode gas injection.

The present two-temperature code and a previous single-temperature version[25] of the model were used to predict the performance of the extended anode MPD thruster. Calculated and experimental thrust values are plotted in Figure 4, measured total voltage-current and predicted plasma voltage-current characteristics are shown in Figure 5, and predicted flow efficiencies are displayed in Figure 6. Both models predict the thrust fairly accurately, but diverge from the experimental values at currents approaching 21 kA (dashed vertical line in Figure 4). No steady-state solution was obtained with the two-temperature model for discharge currents above this value. The predicted plasma potentials correctly reproduce the trend of the experimentally measured voltage-current characteristics, but are consistently lower by approximately 40 volts, reflecting the lack of electrode fall calculations in both models. The slightly higher flow efficiencies predicted by the two-temperature model result from the more accurate calculation of the transport coefficients, which primarily impact the viscous loss terms (through the coefficient of viscosity, Eqn. 16) and the predicted plasma voltage drop (via the electrical conductivity, Eqn. 7a). The single temperature model overestimates the viscosity coefficient, which depends upon the (typically lower) ion temperature, and underestimates the electrical conductivity, which is a function of the (typically higher) electron temperature. For the cases considered, the viscous drag is small compared to the total thrust (typically less than 1%), and may be neglected. However, the higher electrical conductivity lowers the predicted plasma potential (and consequently the power deposited in the plasma), hence for similar thrusts the calculated flow efficiencies are somewhat higher. For the two-temperature model, the flow efficiency increases from 40% at 10 kA to around 50% at 21 kA, at which point steady-state convergence could not be obtained. As discussed earlier, the flow efficiency significantly overestimates the total thruster efficiency. The calculated plasma voltage at 20 kA is 17 volts (Figure 5), yielding a flow efficiency (Eqn. 46) of nearly 50%; however, the measured discharge voltage is approximately 70 volts, yielding a total thruster efficiency of only 15%. Such discrepancies underscore the need to develop and incorporate accurate electrode fall models into MPD thruster simulations.

Both the one-temperature and two-temperature self-field models assume uniform gas injection at the backplate, which corresponds most closely to the 50:50 propellant split used in the experiments. As noted above, the onset of thruster instability was reported at a discharge current of approximately 21 kA using 50:50 gas injection. The lack of steady-state convergence in the two-temperature model for discharge currents exceeding the onset current was not anticipated, and an attempt was made to determine if such an effect

occurred when modeling other cylindrical geometry thrusters. Two thruster geometries were selected from the extensive set of experimental onset parameters catalogued by Preble.[10] The first thruster had a cathode with a radius of 0.95 cm and a length of 5.8 cm, and an anode with an inner radius of 5.1 cm and a length of 6.0 cm. The argon propellant was injected with a 50:50 split at a mass flow rate of 6 g/s. The onset of thruster instability was experimentally measured at a discharge current of around 19-20 kA, corresponding to a $J^2/\dot{m}$ value of 6.0-7.0 $\times 10^{10}$ A^2-s/kg. The second thruster consisted of a cathode with a radius of 0.47 cm and a length of 3.2 cm, and an anode with an inner radius of 2.8 cm and a length of 3.2 cm, operated with an argon mass flow rate of 3 g/s. The onset of instability for this thruster occurred at a discharge current of approximately 15-16 kA, corresponding to a $J^2/\dot{m}$ value of approximately $7.5 - 8.5 \times 10^{10}$ A^2-s/kg. The two-temperature model was run for both thruster geometries over a range of $J^2/\dot{m}$ values, with the results shown in Figure 7. The solid data points denote converged steady-state code solutions, and the open data points signify the range of performance variation obtained as the code attempted to find a steady-state solution. The dashed vertical lines represent the experimentally determined minimum and maximum values of the onset current for the two thrusters, which varied due to the method of propellant injection and slight adjustments to the cathode lengths. In general, the model does not converge for onset parameters within 20% of the experimentally determined values. This is rather remarkable, as the single-fluid equations do not support plasma instabilities, and the propellant is already assumed to be fully ionized. Numerically, the lack of convergence appears in the set of fluid equations, characterized by oscillations in both the ion and electron temperatures and the fluid density values (which are manifested in the calculated plasma potentials and exhaust velocities, preventing the numerical convergence criteria from being satisfied). It is possible that the plasma conditions leading to thruster onset can be modeled within the single-fluid approximations, but where the plasma would dissipate energy via instability processes, the model instead simply oscillates about a steady-state solution. The incorporation of additional energy dissipation mechanisms, such as higher-order ionization or microinstability effects, may thus provide significant insight into the mechanisms responsible for the onset of thruster instabilities,[20,30,31] and requires further investigation.

Geometric Scaling Analysis

A limited set of computer runs were performed to assess the effect of geometric scale changes on self-field MPD thruster performance. Table 1 lists the matrix of cylindrical thruster geometries chosen for comparison. The first geometry set (MPDT-1) consisted of a 0.5 cm radius cathode, surrounded by a 2.5 cm radius anode. The second set (MPDT-2) doubled the anode radius to 5.0 cm, but kept the cathode radius at 0.5 cm. The third set kept the anode radius at 5.0 cm, but increased the cathode radius to 1.0 cm. For each combination of radii, the electrode lengths were scaled from 1 to 5 times the anode radius (with equal anode and cathode lengths assumed), yielding 15 cylindrical thruster geometries. The argon propellant mass flow rate was kept constant at 1 g/s, and was assumed to be fully ionized for all cases. Four $J^2/\dot{m}$ values, ranging from 2.5×10^{10} A^2-s/kg to 1.0×10^{11} A^2-s/kg, were evaluated for each geometry. Results of the numerical simulations for each thruster geometry are presented below.

MPDT-1. Thrust characteristics for the 2.5 cm anode radius, 0.5 cm cathode radius thruster are presented in Figure 8a. The thrust remains fairly constant with increasing electrode length for $J^2/\dot{m}$ values of 2.5×10^{10}A^2-s/kg and 5.0×10^{10}A^2-s/kg. At $J^2/\dot{m}$=7.5×10^{10}A^2-s/kg the thrust remains fairly constant for l_a/r_a (anode length to anode radius) values less than 3; however, steady-state solutions could not be obtained for $l_a/r_a \geq 4$. Only one steady-state solution was found for $J^2/\dot{m}$=1.0×10^{11}A^2-s/kg, at $l_a/r_a = 1$; the model would not converge for larger electrode lengths. The maximum thrust of 16.5 N occurs for l_a/r_a and $J^2/\dot{m} = 1.0 \times 10^{11}$ A^2-s/kg, corresponding to a specific impulse of 1680 seconds.

If a lack of convergence in the steady-state code does reflect unstable thruster operation, as discussed in previous sections, then it would appear for this geometry that higher $J^2/\dot{m}$ values drive the design toward shorter electrode lengths, with optimal l_a/r_a ratios of around unity. It is thus tempting to conclude that

l_a/r_a ratios should be kept at unity for this thruster under all operating conditions; however, competing with this effect is the requirement for high flow efficiencies. Figure 8b plots the flow efficiency versus l_a/r_a as a function of $J^2/\dot{m}$. At 2.5×10^{10}A^2-s/kg, the flow efficiency dramatically increases with increasing thruster length from roughly 48% at $l_a/r_a = 1$ to over 60% at $l_a/r_a = 5$, where the flow efficiency begins to level off. The increasing efficiency is due primarily to a decrease in the calculated plasma potentials (Figure 8c); longer electrodes provide a lower current density, which decreases the electric field and lowers the plasma potential. At the higher $J^2/\dot{m}$ value of 5.0×10^{10}A^2-s/kg, the flow efficiency increases from roughly 63% at $l_a/r_a = 1$ to around 68% at $l_a/r_a = 2$, after which the efficiency remains fairly constant with increasing thruster length. At the still higher $J^2/\dot{m}$ value of 7.5×10^{10}A^2-s/kg, the flow efficiency only slightly increases with increasing electrode length, and the simulation was unable to converge for $l_a/r_a \geq 4$. The efficiency at $J^2/\dot{m} = 1.0 \times 10^{11}$A^2-s/kg and $l_a/r_a = 1$ was approximately 65%, comparable to the efficiency obtained at $J^2/\dot{m} = 7.5 \times 10^{10}$A^2-s/kg for the same l_a/r_a ratio. Steady-state convergence was not possible for $J^2/\dot{m} = 1.0 \times 10^{11}$A^2-s/kg and $l_a/r_a \geq 2$. As noted previously, a trade-off must thus be made between efficient operation at lower $J^2/\dot{m}$ values, which requires longer electrode lengths, and thruster stability requirements, which drive the electrode design toward shorter electrode lengths for higher values of $J^2/\dot{m}$.

MPDT-2. The second geometry set chosen for simulation retained the same cathode radius of 0.5 cm, but doubled the anode radius from 2.5 cm to 5.0 cm for a thruster aspect ratio of 10. The steady-state code was able to converge for only a few operating conditions, as illustrated in Figures 9a through 9c. Convergence was obtained for $J^2/\dot{m}$ values of 2.5×10^{10}A^2-s/kg when $l_a/r_a \leq 3$, and 5.0×10^{10}A^2-s/kg when $l_a/r_a = 1$. Convergence could not be obtained for higher $J^2/\dot{m}$ values, even with the shorter electrode lengths. Thrust (Figure 9a) decreases with increasing electrode length at the lower $J^2/\dot{m}$ value, while the flow efficiency (Figure 9b) remains constant out to $l_a/r_a = 2$, after which the flow efficiency also declines. The maximum calculated thrust, at $l_a/r_a = 1$ and $J^2/\dot{m}=5.0\times10^{10}$A^2-s/kg, was approximately 16 N, corresponding to a specific impulse of roughly 1630 s. These results indicate that, for this larger aspect ratio thruster, shorter electrodes are preferable under all operating conditions. The flow efficiency in the stable operating regions is approximately 75%, higher than the flow efficiencies found under similar operating conditions in MPDT-1. Unfortunately, MPDT-2 appears to be limited to rather low values of $J^2/\dot{m}$ before the onset of thruster instability, and because specific impulse scales as $J^2/\dot{m}$, the utility of such a device would be greatly restricted. The reduced stability of this large aspect ratio thruster agrees with the general results of Preble's onset analysis,[10] which found that smaller aspect ratio thrusters achieved higher values of $J^2/\dot{m}$ before the onset of thruster voltage oscillations.

MPDT-3. The third set of geometries investigated, MPDT-3, retained the larger anode radius of 5.0 cm but doubled the cathode radius to 1.0 cm, returning the thruster aspect ratio to 5. Predicted thrust, voltage, and flow efficiencies versus l_a/r_a are plotted in Figures 10a through 10c as functions of $J^2/\dot{m}$. The reduction in aspect ratio increased the parameter space for steady-state code convergence, indicating that stable thruster performance may be obtained over a wider range of operating conditions for small aspect ratio thrusters (in agreement with Preble's onset survey). Thrust values for the lower $J^2/\dot{m}$ values agree fairly well with the thrust values predicted for MPDT-1, which is to be expected for self-field thrusters with similar aspect ratios. However, only one steady-state solution was obtained for MPDT-3 at $J^2/\dot{m}=5.0\times10^{10}$A^2-s/kg, at $l_a/r_a = 1$, and no steady-state solution was obtained at $J^2/\dot{m}=1.0\times10^{11}$A^2-s/kg. Although the aspect ratios were the same, the larger electrode radii in MPDT-3 reduced the stable operating regime of the thruster. Additional differences are observed in the flow efficiencies of each thruster. Whereas the flow efficiency steadily increased with l_a/r_a at $J^2/\dot{m}=2.5\times10^{10}$A^2-s/kg in MPDT-1, the flow efficiency increased and peaked at $l_a/r_a=4$ in MPDT-3, after which the flow efficiency decreased with increasing electrode length. At $J^2/\dot{m}=5.0\times10^{10}$A^2-s/kg, the flow efficiency increased in MPDT-1 until $l_a/r_a=2$, after which the flow efficiency remained approximately constant. However, the flow efficiency steadily decreased in MPDT-3 with increasing electrode length under the same operating conditions. Both trends may be explained by comparing the thrust (Figure 10a) and plasma voltage values (Figure 10c). At $J^2/\dot{m}=2.5\times10^{10}$A^2-s/kg,

the thrust remains fairly constant from $l_a/r_a = 1$ to 4, then drops approximately 5% as l_a/r_a is increased from 4 to 5. The voltage, however, drops almost 30% as l_a/r_a increases from 1 to 4, then remains fairly constant as l_a/r_a changes from 4 to 5. Referring to Equation 46, the nearly constant thrust, coupled with the decreasing plasma voltage, results in an increasing plasma flow efficiency for $1 \leq l_a/r_a \leq 4$. As l_a/r_a is increased to 5, the plasma voltage levels off and the thrust decreases, resulting in a lower plasma flow efficiency. At $J^2/\dot{m}$=5.0×10^{10}A^2-s/kg, both the thrust and plasma voltage are decreasing with increasing l_a/r_a in such a manner that the plasma flow efficiency decreases with increasing l_a/r_a as well. It is of interest to note that MPDT-1 is the half-scale counterpart of MPDT-3, and in partial agreement with Gilland's results[11] the performance of these half-scale and full-scale thrusters are indeed similar for a limited parameter space. However, for these cylindrical self-field thrusters, the similarity in performance starts to diverge at higher values of $J^2/\dot{m}$ and larger values of l_a/r_a, even though the mass flow rates were equivalent. The maximum calculated thrust for MPDT-3 was roughly 14 N for $l_a/r_a = 1$ and $J^2/\dot{m}$=7.5×10^{10}A^2-s/kg, which corresponds to a maximum specific impulse impulse of approximately 1430 s.

Stability Diagrams. Based on the preceding results, stability diagrams were generated for the three sets of thruster geometries (MPDT-1 through 3) as a function of l_a/r_a versus $J^2/\dot{m}$ (Figures 11-13). Regions of steady-state code convergence are depicted as "stable", and nonconvergent regimes as "unstable". Regions without data were left unshaded. Though limited in extent, fairly definite patterns emerge from the diagrams. In general, the thruster simulations were nonconvergent at higher values of $J^2/\dot{m}$ and larger values of l_a/r_a, with the effects becoming more pronounced for the larger aspect ratio thruster. The smaller diameter thruster (MPDT-1) had the largest stable operating space, followed by MPDT-3 (same aspect ratio, but twice the size) and MPDT-2 (with the same anode diameter as MPDT-3 but twice the aspect ratio). Of particular interest are the slopes of the lines denoting stable operation; the slopes are identical for MPDT-1 and MPDT-2, which had identical cathode radii but different aspect ratios. The stability region for MPDT-3, in which the cathode radius was doubled, has twice the slope of the other stability regions, even though the aspect ratios of MPDT-1 and MPDT-3 are identical. In addition, the maximum value of $J^2/\dot{m}$ for stable operation was lower for the larger diameter thruster (MPDT-3) with the same aspect ratio as the smaller thruster (MPDT-1), and was halved when the thruster aspect ratio was doubled (MPDT-2 versus MPDT-1).

These intriguing correlations prompted an attempt to derive a stability scaling relation for the three thruster geometries, and a scaling relation was found of the form:

$$\left(\frac{J^2}{\dot{m}}\right)_c \leq \frac{6.25 \times 10^9}{r_c}\left(\frac{l_c}{l_a}\right)\left[5 - \left(\frac{l_a}{r_a}\right) + 4\left(\frac{10r_c - r_a}{2.5}\right)\right] \quad A^2 - s/kg \tag{47}$$

where $\left(J^2/\dot{m}\right)_c$ denotes the maximum $J^2/\dot{m}$ value (in A^2-s/kg) for stable thruster operation and r_a, l_a, r_c, and l_c are the anode radius and length and cathode radius and length, respectively, measured in centimeters. The inverse scaling with cathode radius is apparent from the stability diagrams, and the factors of 5 and 10 appearing in the expression are apparently related to the maximum values of l_a/r_a and r_a/r_c used in this limited study. The remaining terms are not intuitively obvious, however, and an effort was undertaken to determine the validity of the scaling relation for other cylindrical self-field thrusters. Once again, the extensive data base compiled by Preble[10] proved invaluable for this task. A comparison of experimentally determined onset values with the values predicted by Eqn. 47 are listed in Table 2 for thruster geometries which fall within the geometric constraints of the model: straight, cylindrical self-field thrusters, with uniform argon propellant injection, which satisfy the conditions $l_a/r_a \leq 5$, $r_a/r_c \leq 10$, $r_a \geq 2.54$ cm, $r_c \geq 0.5$ cm, and approximately equal electrode lengths ($l_a \simeq l_c$). The numerical simulations assumed equal electrode lengths, and the factor of (l_c/l_a) in Eqn. 47 arises from an examination of the Preble data set. In general, the predictions of Eqn. 47 and the experimental data agree fairly well, with better conformity at shorter length electrodes. Thus, for thruster geometries which fall within the geometric constraints outlined above, the stability scaling relationship may be useful as a predictor of thruster instability.

The above scaling relation was used to predict the stability performance of an MPD thruster with a cathode radius of 1 cm and anode radius of 10 cm, the full-scale counterpart to the MPDT-2 thruster above (with an aspect ratio of 10). Based on the above results for MPDT-2, a value of $l_a/r_a = 1$ was chosen to improve the region of operational stability. Inserting values for r_a, r_c, and l_a/r_a into Eqn. 47 yields a maximum $J^2/\dot{m}$ value of 2.5×10^{10}A^2-s/kg for stable code convergence (and, based on the previous arguments, thruster stability). The two-temperature model was then used to simulate the thruster, with a mass flow rate of 1 g/s (argon) and discharge currents of 5 kA and 7.5 kA; the model converged to a steady-state solution for the 5 kA discharge current, but did not converge for the 7.5 kA value. The mass flow was then raised to 4 g/s, with discharge currents of 10 kA and 14 kA; the simulation converged for the lower discharge current, but no steady-state solution could be obtained for the higher value. The thruster geometry was then changed, keeping the anode and cathode radii the same but extending l_a/r_a to 3. The stability equation predicts a maximum $J^2/\dot{m}$ value of 1.25×10^{10}A^2-s/kg. The code was operated with a mass flow rate of 1 g/s at discharge currents of 3.5 kA and 5 kA; the model converged for the lower discharge current but not for the higher value. It must be reiterated that the above results only show that the stability equation, based upon the performance of a numerical model, can predict the stable regions of model operation; it is the somewhat tenuous association between steady-state model convergence and experimentally measured onset data that allows such speculation concerning stable thruster operating regimes.

Based on the above results, and their associated limitations, the following observations may now be tentatively added to the list of maxims discussed in the introduction. For cylindrical self-field MPD thrusters, operated on argon and satisfying the geometric constraints listed above, stable operation at higher values of $J^2/\dot{m}$ requires smaller ratios of l_a/r_a. At lower values of $J^2/\dot{m}$, longer electrodes are required to increase the thruster flow efficiency. Smaller aspect ratio thrusters are generally more stable than larger aspect ratio thrusters of equivalent anode diameter, and larger aspect ratio thrusters require shorter electrode lengths for stable operation. Smaller diameter thrusters are in general more stable over a wider range of operating conditions than their large-scale geometric counterparts. These preliminary results are based on a very limited set of numerical data, and such important effects as partial versus full ionization, nonequivalent anode and cathode lengths, nonuniform propellant injection, different propellant species, and the effects of flared anode geometries (to name but a few) remain to be investigated.

IV. Concluding Remarks

A two-dimensional, two-temperature, single fluid magnetohydrodynamics code was developed to predict steady-state, self-field MPD thruster performance. The governing equations and numerical methods of solution were outlined and discussed. Experimental comparisons with the Princeton extended anode MPD thruster were used to benchmark model predictions. The model accurately predicts thrust and reproduces trends in the discharge voltage for discharge currents below experimentally measured onset values. However, because the model does not include electrode effects the calculated voltage drops are significantly lower than experimentally measured values. Predictions of thrust and flow efficiency are made for a matrix of 15 cylindrical thruster geometries over a range of $J^2/\dot{m}$ values, assuming fully ionized argon propellant with a mass flow rate of 1 g/s in each case. The simulations indicate that thruster operation at high values of $J^2/\dot{m}$ requires short electrode lengths for stable operation. At lower values of $J^2/\dot{m}$, longer electrodes are required to improve the thruster flow efficiency. Small aspect ratio thrusters are in general more stable than larger aspect ratio thrusters of equivalent anode diameter, and larger aspect ratio thrusters require shorter electrode lengths for stable operation. Smaller diameter thrusters are generally more stable over a wider range of operating conditions than their large-scale geometric counterparts. A maximum specific impulse of 1680 s was achieved with a 2.5 cm anode radius, 0.5 cm cathode radius thruster with $l_a/r_a = 1$ operated at $J^2/\dot{m} = 1.0 \times 10^{11}$ A^2-s/kg. A scaling relation to predict the onset of self-field thruster instability as a function of geometry was derived and tested against published onset data. Within the constraints imposed by the model, the scaling relation could generally predict onset to within 20% of the experimental values.

References

1. Seikel, G. R., York, T. M., and Condit, W. C., "Applied-Field Magnetoplasmdynamic Thrusters for Orbit-Raising Missions", in *Orbit-Raising and Maneuvering Propulsion: Research Status and Needs*, Caveny, L. H. (ed), Progress in Astronautics and Aeronautics, vol. 89, 1984, pp. 260-286.

2. Gilland, J. H., Myers, R. M., and Patterson, M. J., "Multimegawatt Electric Propulsion System Design Considerations", AIAA Paper No. 90-2552, July 1990.

3. Myers, R. M., Mantenieks, M. A., and LaPointe, M. R., "MPD Thruster Technology", AIAA Paper No. 91-3568, Sept. 1991.

4. Sovey, J. S., and Mantenieks, M. A., "Performance and Lifetime Assessment of MPD Arc Thruster Technology", AIAA Paper No. 88-3211, July 1988.

5. Nerheim, N. M., and Kelly, A. J., "A Critical Review of the State-of-the Art of the MPD Thrustor", AIAA Paper No. 67-688, Sept. 1967.

6. Tahara, H., Yaasui, H., Kagaya, Y., and Yoshikawa, T., "Experimental and Theoretical Researches on Arc Structure in a Self-Field Thruster", AIAA Paper No. 87-1093, May 1987.

7. Hugel, H., "Effect of Self-Magnetic Forces on the Anode Mechanism of a High Current Discharge", *IEEE Transactions on Plasma Science*, **PS-8**(4), December 1980, pp. 437-442.

8. Lawless, J. L., and Subramaniam, V. V., "Theory of Onset in Magnetoplasmadynamic Thrusters", *J. Propulsion and Power*, **3**(2), March-April 1987, pp. 121-127.

9. Subramaniam, V. V. and Lawless, J. L., "Electrode-Adjacent Boundary Layer Flow in Magnetoplasmadynamic Thrusters", *Phys. Fluids*, **31**(1), January 1988, pp. 201-209.

10. Preble, J. C., "Onset in Magnetoplasmadynamic Thrusters: A Model of an Electrothermal Instability", M.S. Thesis, Department of Aeronautics and Astronautics, Massachusetts Institute of Technology, May 1990.

11. Niewood, E., Preble, J., Hastings, D., and Martinez-Sanchez, M., "Electrothermal and Modified Two Stream Instabilities in MPD Thrusters", AIAA Paper No. 90-2607, July 1990.

12. Wagner, H. P., Auweter-Kurtz, M., Roesgen, T., Messerschmid, E. W., and Kaeppeler, H. J., "Gradient Driven Instabilitie in Stationary MPD Thruster Flows", AIAA Paper No. 90-2603.

13. King, D. Q., "Magnetoplasmadynamic Channel FLow for Design of Coaxial MPD Thrusters", Ph. D. Dissertation No. 1544-T, Department of Mechanical and Aerospace Engineering, Princeton University, Princeton, NJ, December 1981.

14. Gilland, J. H., "The Effect of Geometrical Scale Upon MPD Thruster Behavior", M.S. Thesis No. 1811-T, Department of Mechanical and Aerospace Engineering, Princeton University, Princeton, NJ, March 1988.

15. Schmidt, W. M., "Effects of Scaling on the Performance of Magnetoplasmadynamic Thrusters", Engineer's Thesis, Naval Postgraduate School, Monterey, CA., June 1989.

16. Cassady, R. J., Stoyanof, D. S., and Kilgore, O. W., "Characterization of Performance Variation with Geometry in an MPD Thruster", IEPC Paper No. 85-2021, 1985.

17. Heimerdinger, D. J., and Martinez-Sanchez, M., "Fluid Dynamics in a Magnetoplasmadynamic Thruster", IEPC Paper No. 88-039, presented at the 20th International Electric Propulsion Conference, Garmisch-Partenkirchen, West Germany, October 6-8, 1988.

18. Martinez-Sanchez, M., "Structure of Self-Field Accelerated Plasma Flows", *J. Propulsion and Power*, **7**(1), Jan-Feb 1991, pp.56-64.

19. Kunii, Y., Shimuzu, Y., and Kuriki, K., "Current Distribution in a Quasisteady MPD Arcjet with Various Anode Geometries", *AIAA Journal*, **22** (6), June 1984, pp. 750-751.

20. Uematsu, K., Mori, K., Kuriki, K., and Kuninaka, H., "Effect of Electrode Configuration on MPD Arcjet Performance", IEPC Paper No. 84-11, presented at the 17th International Electric Propulsion Conference, Tokyo, Japan, may 28-31, 1984.

21. Lefever-Button, G., and Subramaniam, V. V., "Quasi One-Dimensional MPD Flows", IEPC Paper No. 91-061, presented at the 22nd International Electric Propulsion Conference, Viareggio, Italy, October 14-17, 1991.

22. Choueiri, E. Y., "Electron-Ion Streaming Instabilities of an Electromagnetically Accelerated Plasma", Ph.D. Dissertation, Department of Mechanical and Aerospace Engineering, Princeton University, Princeton, NJ, October 1991.

23. Choueiri, E. Y., Kelley, A. J., and Jahn, R. G.,"Current Driven Instabilities of an Electromagnetically Accelerated Plasma", IEPC Paper No. 88-042, presented at the 20^{th} International Electric Propulsion Conference, October 3-6, 1988, Garmisch-Partenkirchen, W. Germany.

24. Tilley, D. L., "An Investigation of Microinstabilities in a kW Level Self-Field MPD Thruster", M.S. Thesis No. 1917-T, Department of Mechanical and Aerospace Engineering, Princeton University, Princeton, NJ, October 1991.

25. LaPointe, M. R., "Numerical Simulation of Self-Field MPD Thrusters", AIAA Paper No. 91-2341, June 1991; see also NASA CR-187168, August 1991.

26. Sutton, G. W., and Sherman, A., *Engineering Magnetohydrodynamics*, McGraw-Hill Book Co., New York, 1965.

27. Mitchner, M., and Kruger, C. H. Jr., *Partially Ionized Gases*, Wiley-Interscience, 1973.

28. Greenspan, D. G., *Discrete Numerical Methods in Physics and Engineering*, Academic Press, New York, 1974.

29. Wolff, M., "A High Performance Magnetoplasmadynamic Thruster", M.S. Thesis No. 1632-T, Department of Mechanical and Aerospace Engineering, Princeton University, Princeton, NJ, 1983.

30. Caldo, G., Choueiri, E. Y., Kelly, A. J., and Jahn, R. G., "An MPD Code with Anomalous Transport", IEPC Paper No. 91-102, presented at the 22nd International Electric Propulsion Conference, October 14-17, 1991, Viareggio, Italy.

31. Sleziona, P. C., Auweter-Kurtz, M., and Schrade, H. O., "MPD Thruster Calculation Considering High Ionization Modes", presented at the 22nd International Electric Propulsion Conference, October 14-17, 1991, Viareggio, Italy.

MODEL GEOMETRY		$J^2/\dot{m}$ (10^9 A^2-s/kg) 2.5	5.0	7.5	10.0
MPDT-1	l_a/r_a				
	1	S	S	S	S
r_a=2.5 cm	2	S	S	S	U
r_c=0.5 cm	3	S	S	S	U
r_a/r_c=5	4	S	S	U	U
	5	S	S	U	U
MPDT-2	l_a/r_a				
	1	S	S	U	U
r_a=5.0 cm	2	S	U	U	U
r_c=0.5 cm	3	S	U	U	U
r_a/r_c=10	4	U	U	U	U
	5	U	U	U	U
MPDT-3	l_a/r_a				
	1	S	S	S	U
r_a=5.0 cm	2	S	S	U	U
r_c=1.0 cm	3	S	S	U	U
r_a/r_c=5	4	S	S	U	U
	5	S	S	U	U

Table 1. Matrix of thruster geometries and $J^2/\dot{m}$ values used in numerical simulations. r_a, r_c, and l_a denote anode radius, cathode radius, and electrode length, respectively. "S" denotes steady-state solutions, "U" denotes lack of steady-state code convergence. All data for $\dot{m}$ = 1 g/s, Ar.

PREBLE ENTRY #	r_a (cm)	r_c (cm)	l_a (cm)	l_c (cm)	$J^2/\dot{m}$ (10^9 A^2-s/kg)	
					EXPT	EQN. 47
1	2.8	0.5	3.2	3.2	88	92
19	5.1	0.95	6.0	1.7	23	20
26	5.1	0.95	6.0	2.3	28	27
15	5.1	0.95	6.0	2.5	43	30
77	5.1	0.95	5.72	2.54	35	32
79	5.1	0.95	5.72	2.54	36	32
27	5.1	0.95	6.0	3.2	38	38
28	5.1	0.95	6.0	4.35	48	52
53	5.1	0.95	6.0	5.0	67	60
23	5.1	0.95	6.0	5.3	80	63
29	5.1	0.95	6.0	5.8	60	69
30	5.1	0.95	6.0	6.91	74	82
31	5.1	0.95	6.0	10.0	74	119
90	5.1	0.95	6.0	10.0	85	119
92	5.1	0.95	6.0	10.0	88	119
16	5.1	0.95	6.0	10.0	88	119
91	5.1	0.95	6.0	10.0	94	119
33	5.1	0.95	6.0	10.0	131	119
86	5.1	0.95	6.0	12.4	88	82
45	5.1	0.95	6.0	10.0	96	80

Table 2. Comparison of experimentally determined onset values (EXPT) with values predicted by stability scaling relation (Equation 47).

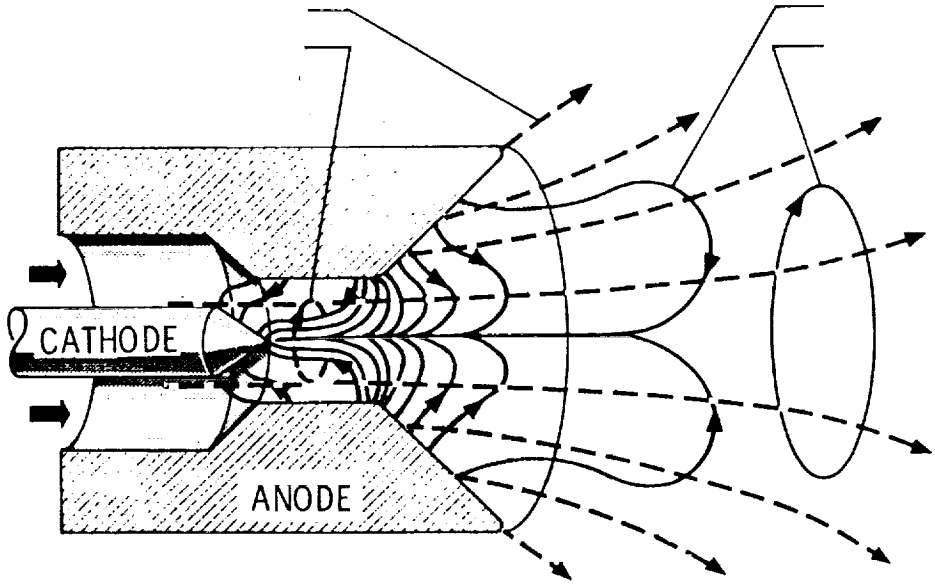

Figure 1. Schematic of a self-field MPD thruster.

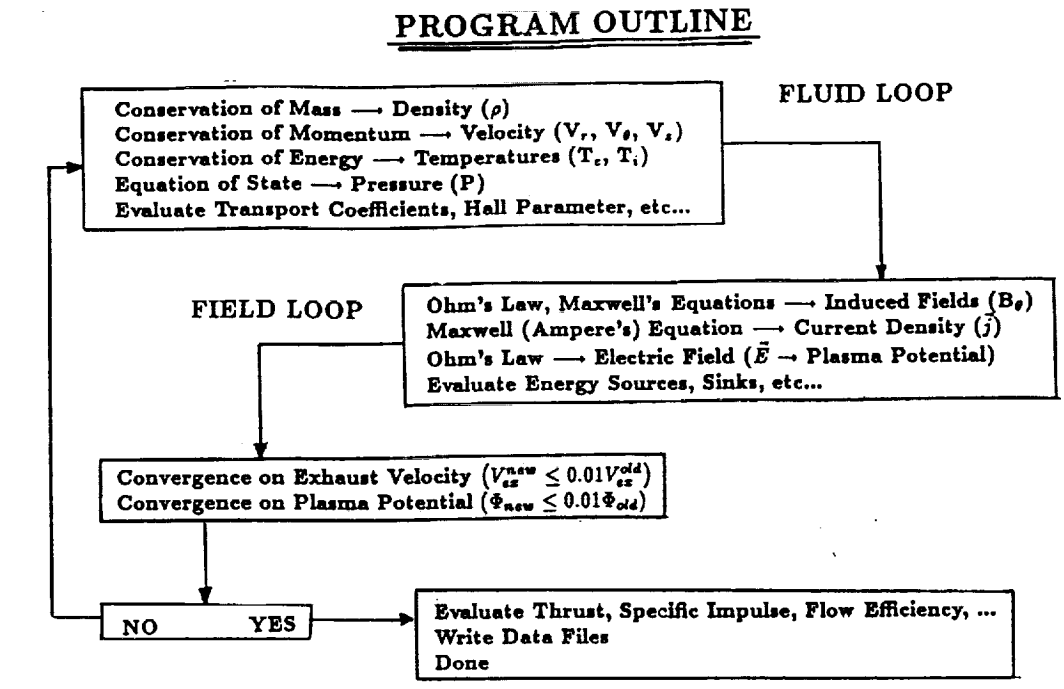

Figure 2. Program outline of MPD thruster numerical simulation.

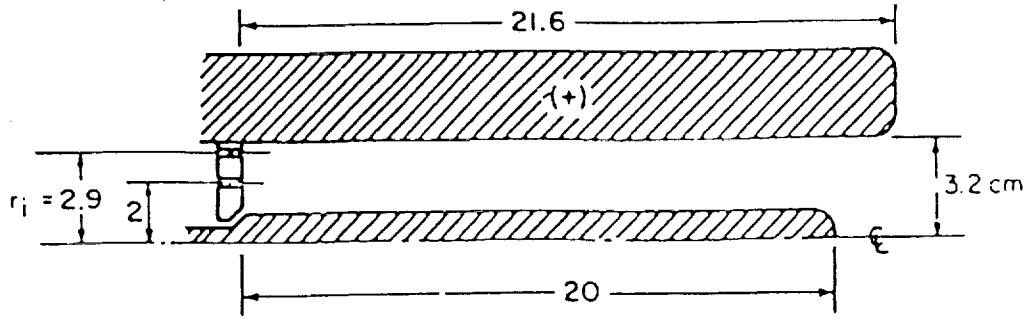

Figure 3. Schematic of Princeton University extended anode MPD thruster[29].

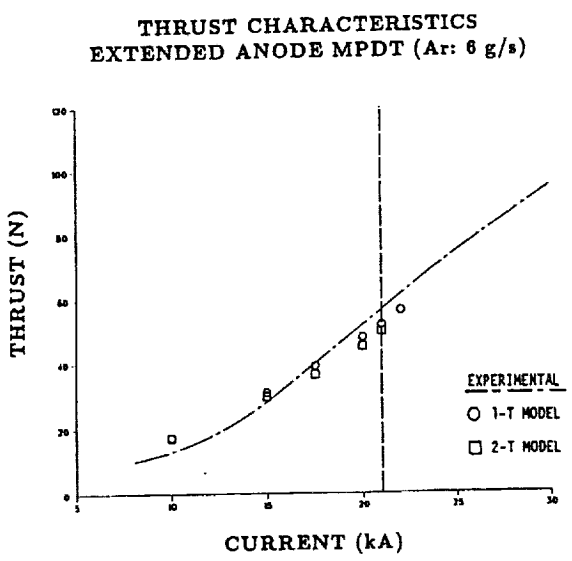

Figure 4. Thrust characteristics for the extended anode MPD thruster, $\dot{m}$ = 6 g/s (Ar). 1-T: single temperature code, 2-T: two-temperature code results. Dashed vertical line corresponds to experimentally measured onset current with 50:50 propellant injection.

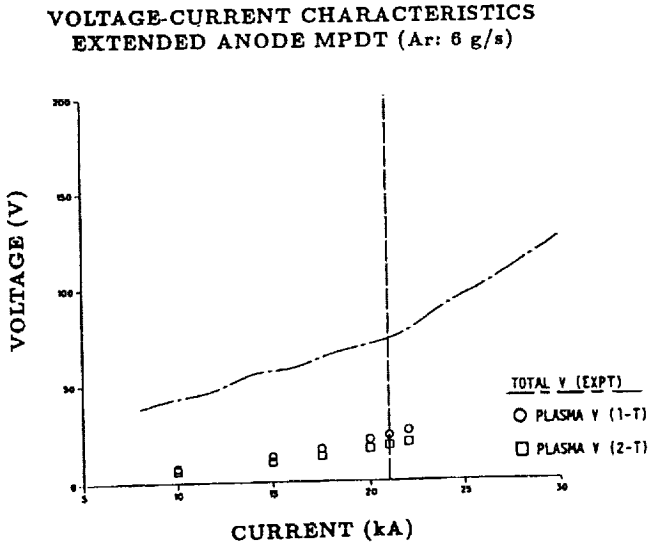

Figure 5. Measured total voltage (⟵ - - ⟶) and calculated plasma voltage (symbols) for the extended anode MPD thruster, $\dot{m}$ = 6 g/s (Ar). 1-T: single temperature code, 2-T: two-temperature code results. Dashed vertical line corresponds to experimentally measured onset current with 50:50 propellant injection.

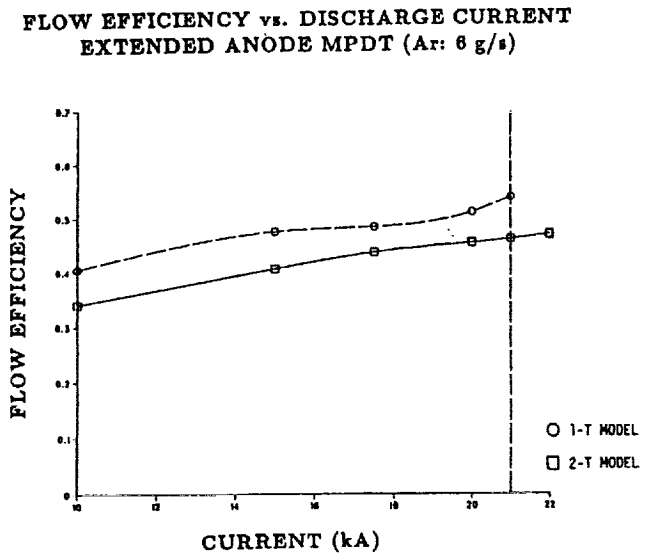

Figure 6. Calculated plasma flow efficiency for the extended anode MPD thruster, $\dot{m}$ = 6 g/s (Ar). 1-T: single temperature code, 2-T: two-temperature code results. Dashed vertical line corresponds to experimentally measured onset current with 50:50 propellant injection.

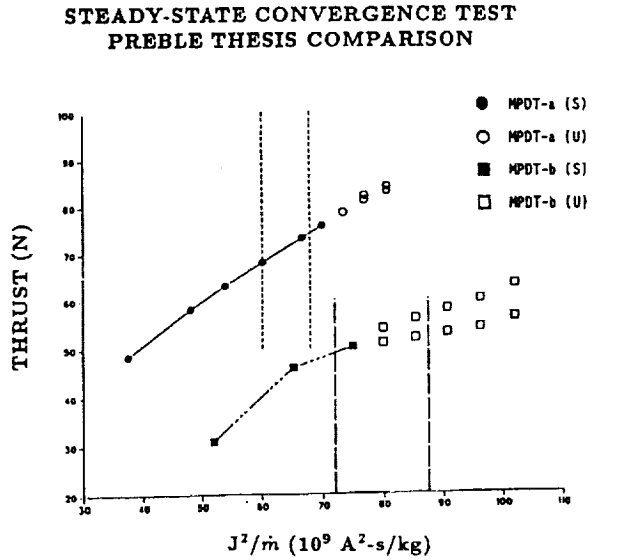

Figure 7. Steady-state, two-temperature model convergence tests. MPDT-a: r_a = 5.1 cm, r_c = 0.95 cm, l_a = 6.0 cm, l_c = 5.8 cm, $\dot{m}$ = 6 g/s (Ar). MPDT-b: r_a = 2.8 cm, r_c = 0.475 cm, l_a = 3.2 cm, l_c = 3.2 cm, $\dot{m}$ = 3 g/s (Ar). Dashed vertical lines correspond to experimentally measured minimum and maximum onset current values. (S): Stable, (U): Unstable code convergence.

MPDT-1: THRUST vs. LENGTH/RADIUS
(r_a = 2.5 cm, r_c = 0.5 cm, 1 g/s Ar)

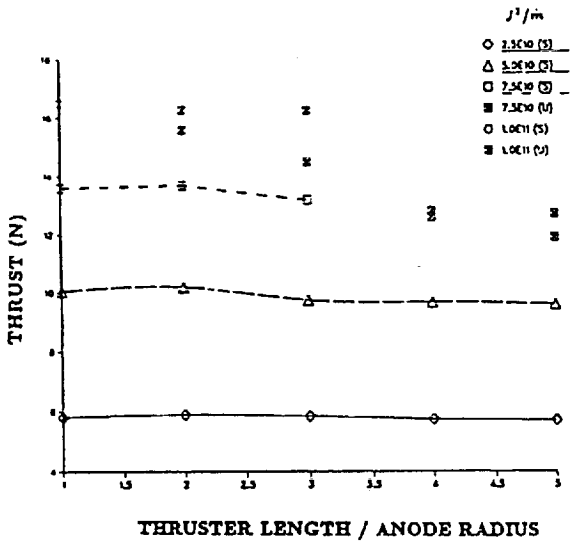

Figure 8(a). Calculated thrust characteristics for MPDT-1. (S): stable, (U): unstable code convergence.

MPDT-1: FLOW EFFICIENCY vs. LENGTH/RADIUS
(r_a = 2.5 cm, r_c = 0.5 cm, 1 g/s Ar)

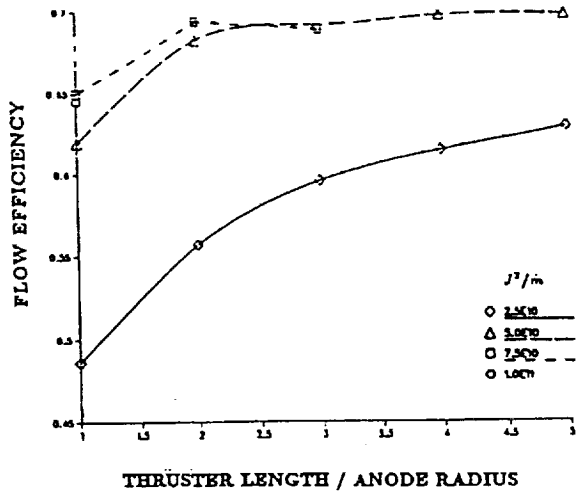

Figure 8(b). Calculated flow efficiencies for MPDT-1 (steady-state solutions).

MPDT-1: VOLTAGE vs. LENGTH/RADIUS
(r_a = 2.5 cm, r_c = 0.5 cm, 1 g/s Ar)

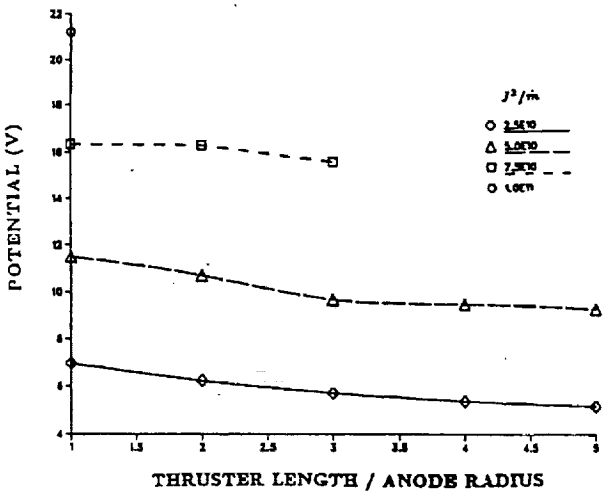

Figure 8(c). Calculated plasma potentials for MPDT-1 (steady-state solutions).

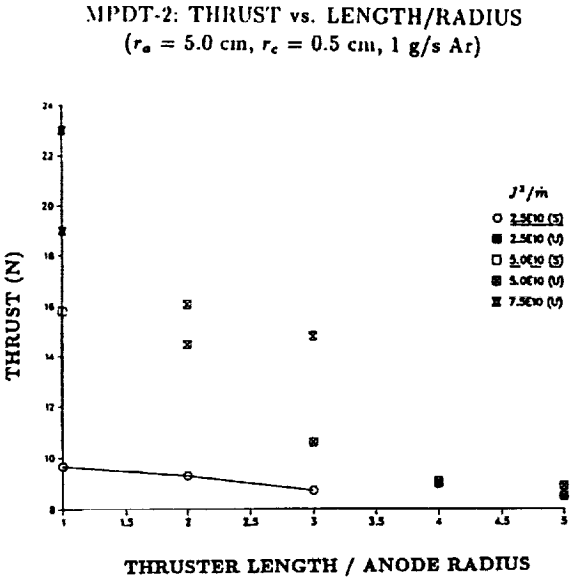

Figure 9(a). Calculated thrust characteristics for MPDT-2. (S): stable, (U): unstable code convergence.

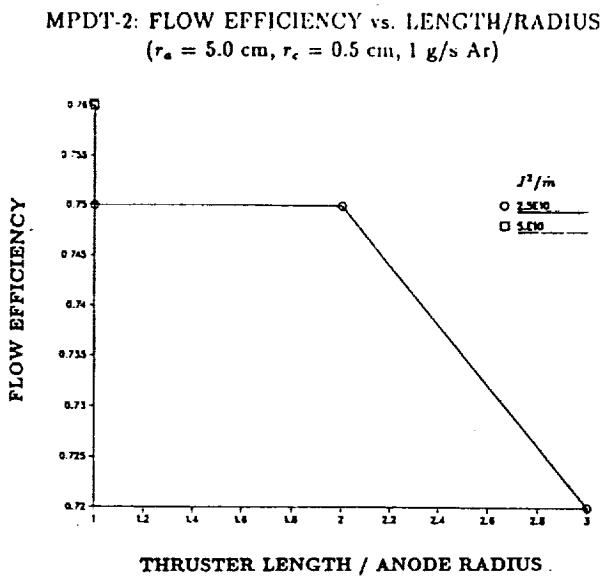

Figure 9(b). Calculated flow efficiencies for MPDT-2 (steady-state solutions).

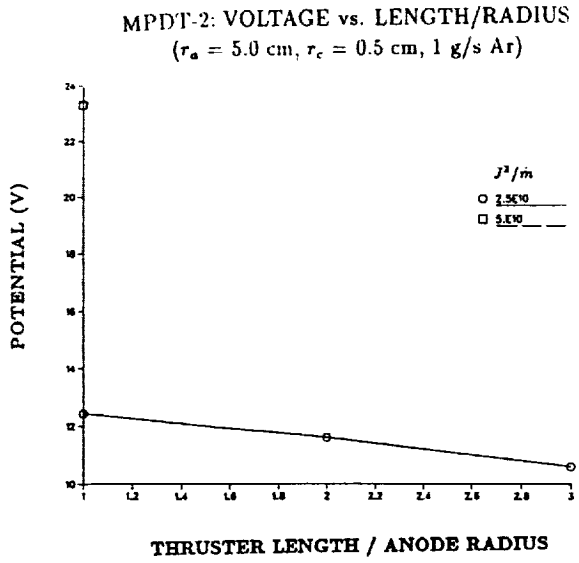

Figure 9(c). Calculated plasma potentials for MPDT-2 (steady-state solutions).

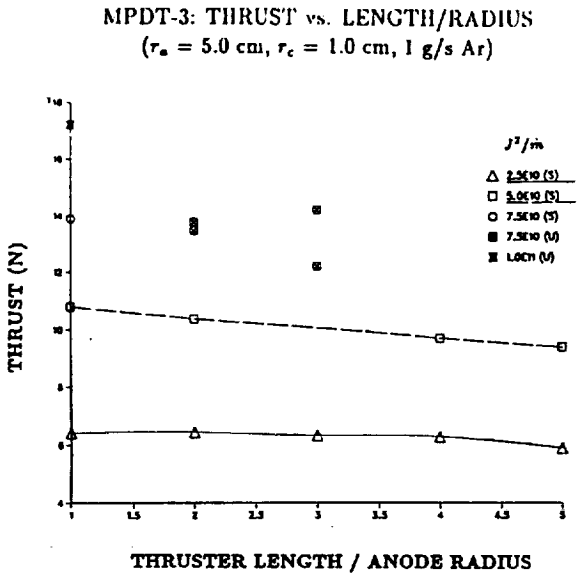

Figure 10(a). Calculated thrust characteristics for MPDT-3 (S): stable, (U): unstable code convergence.

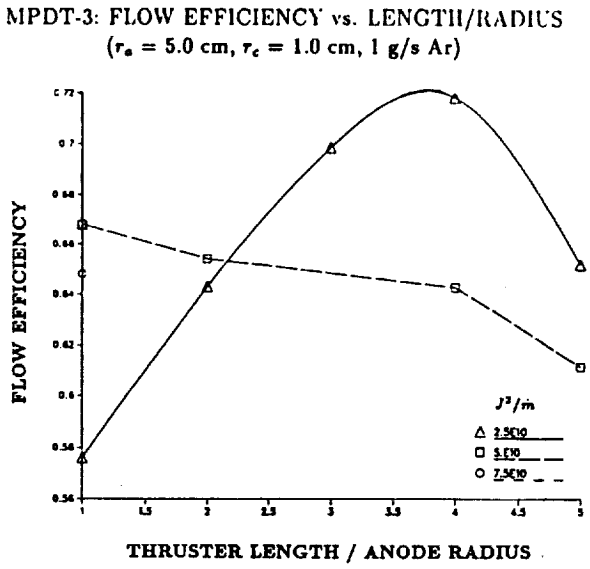

Figure 10(b). Calculated flow efficiencies for MPDT-3 (steady-state solutions).

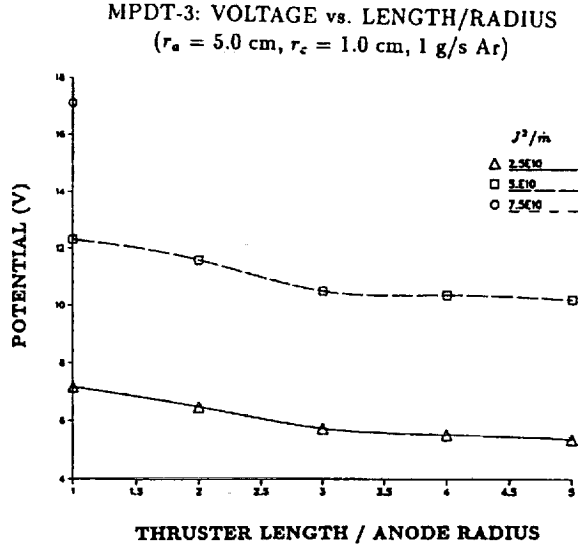

Figure 10(c). Calculated plasma potentials for MPDT-3 (steady-state solutions).

MPDT-1: STEADY-STATE MODEL CONVERGENCE

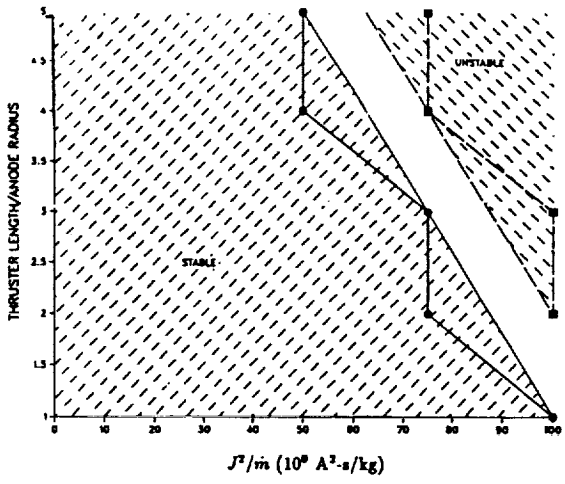

Figure 11. Numerical stability diagram, MPDT-1. Symbols denote numerical data points; "stable" denotes code convergence, "unstable" denotes lack of steady-state convergence. Sloped lines are interpolations to the data points.

MPDT-2: STEADY-STATE MODEL CONVERGENCE

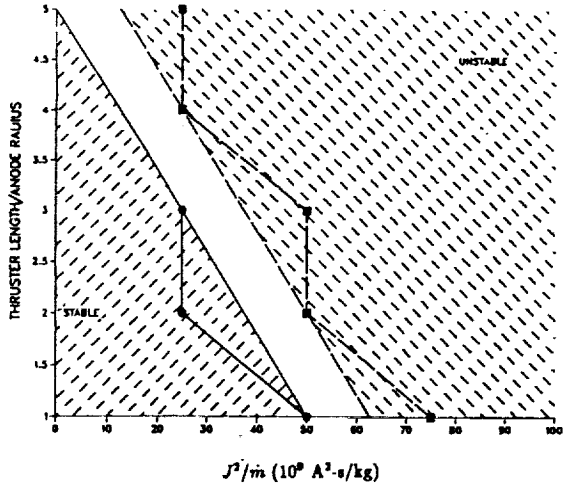

Figure 12. Numerical stability diagram, MPDT-2. Symbols denote numerical data points; "stable" denotes code convergence, "unstable" denotes lack of steady-state convergence. Sloped lines are interpolations to the data points.

MPDT-3: STEADY-STATE MODEL CONVERGENCE

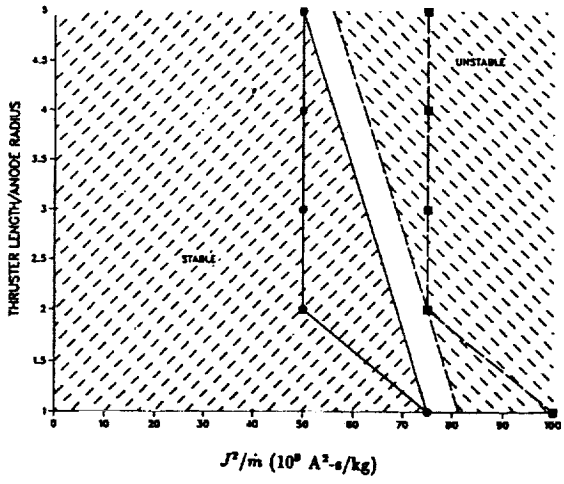

Figure 13. Numerical stability diagram, MPDT-3. Symbols denote numerical data points; "stable" denotes code convergence, "unstable" denotes lack of steady-state convergence. Sloped lines are interpolations to the data points.

REPORT DOCUMENTATION PAGE

Form Approved
OMB No. 0704-0188

1. AGENCY USE ONLY (Leave blank)	2. REPORT DATE	3. REPORT TYPE AND DATES COVERED
	August 1992	Final Contractor Report

4. TITLE AND SUBTITLE

Numerical Simulation of Geometric Scale Effects in Cylindrical Self-Field MPD Thrusters

5. FUNDING NUMBERS

WU-506-42-31

6. AUTHOR(S)

M. LaPointe

7. PERFORMING ORGANIZATION NAME(S) AND ADDRESS(ES)

Sverdrup Technology, Inc.
Lewis Research Center Group
2001 Aerospace Parkway
Brook Park, Ohio 44142

8. PERFORMING ORGANIZATION REPORT NUMBER

E-7277

9. SPONSORING/MONITORING AGENCY NAMES(S) AND ADDRESS(ES)

National Aeronautics and Space Administration
Lewis Research Center
Cleveland, Ohio 44135-3191

10. SPONSORING/MONITORING AGENCY REPORT NUMBER

NASA CR-189224

11. SUPPLEMENTARY NOTES

Project Manager, James S. Sovey, NASA Lewis Research Center, (216) 433-7454. Prepared for the 28th Joint Propulsion Conference and Exhibit cosponsored by the AIAA, SAE, ASME, and ASEE, Nashville, Tennessee, July 6-8, 1992 (work funded by NASA Contract NAS3-25266).

12a. DISTRIBUTION/AVAILABILITY STATEMENT

Unclassified - Unlimited
Subject Category 20

12b. DISTRIBUTION CODE

13. ABSTRACT *(Maximum 200 words)*

A two-dimensional, two-temperature, single fluid magnetohydrodynamics code which incorporates classical plasma transport coefficients and Hall effects has been developed to predict steady-state, self-field MPD thruster performance. The governing equations and numerical methods of solution are outlined and discussed. Experimental comparisons are used to validate model predictions. The model accurately predicts thrust and reproduces trends in the discharge voltage for discharge currents below experimentally measured onset values. However, because the model does not include electrode effects the calculated voltage drops are significantly lower than experimentally measured values. Predictions of thrust and flow efficiency are made for a matrix of fifteen cylindrical thruster geometries assuming a fully ionized argon propellant. A maximum predicted specific impulse of 1680 s is obtained for a thruster with an anode radius of 2.5 cm, a cathode radius of 0.5 cm, and equal electrode lengths of 2.5 cm. A scaling relation is developed to predict, within limits, the onset of cylindrical, self-field thruster instability as a function of geometry and operating condition.

14. SUBJECT TERMS

MPD; Electric propulsion; Numerical simulation

15. NUMBER OF PAGES

28

16. PRICE CODE

A03

17. SECURITY CLASSIFICATION OF REPORT	18. SECURITY CLASSIFICATION OF THIS PAGE	19. SECURITY CLASSIFICATION OF ABSTRACT	20. LIMITATION OF ABSTRACT
Unclassified	Unclassified	Unclassified	